Measurement of radiative pion-proton scattering at backward photon angles*

D. I. Sober, M. Arman,† D. J. Blasberg,‡ R. P. Haddock, K. C. Leung,§ B. M. K. Nefkens, B. L. Schrock||, and J. M. Sperinde¶

Department of Physics, University of California, Los Angeles, California 90024

(Received 30 September 1974)

We have measured the differential cross sections for π^+p and π^-p radiative scattering ($\pi^\pm p \to \pi^\pm p\gamma$) at an incident kinetic energy of 298 MeV with photons produced at very large angles to the incident and scattered particles. The measured photon spectrum extended to 120 MeV. For photon energies below 30 MeV, the results are in agreement with the conventional soft-photon formalism. In the hard-photon region the data fail to reflect the $\Delta(1236)$ resonance in the final state, and are in substantial disagreement with existing theoretical models.

I. INTRODUCTION

The detailed study of pion-proton bremsstrahlung or radiative scattering

$$\pi p \to \pi p \gamma \tag{1}$$

provides information about the following subjects:

(a) the range of validity of the Low soft-photon theorem,

(b) off-mass-shell amplitudes for pion-nucleon scattering, and

(c) the electromagnetic properties of πN resonances.

One can distinguish two different contributions to the bremsstrahlung process: (1) "external" radiation, in which the photon is emitted by one of the incoming or outgoing charged particles [Figs. 1(a)–1(d)]; (2) "internal" radiation, in which the photon is emitted by an intermediate state or at the strong interaction vertex itself [Fig. 1(e)]. The amplitude of external radiation can be calculated using the techniques of quantum electrodynamics.[1] As the center-of-mass photon energy k approaches zero, the bremsstrahlung spectrum has a characteristic $1/k$ dependence.[2] For hadron-hadron scattering the calculation of the bremsstrahlung amplitude is limited by the uncertainty in the treatment of off-mass-shell effects. However, the real difficulty in this case is the calculation of the "internal radiation" contribution to the bremsstrahlung amplitude, in particular in reactions that involve the excitation of a strong resonance, such as the $\Delta^{++}(1236)$.

In view of the asymptotic $1/k$ dependence of the bremsstrahlung amplitude, it is reasonable to expand the amplitude in a power series in the photon energy k as follows:

$$M = a/k + b + ck + \cdots . \tag{2}$$

Low[3] and others[4] have shown that, in the limit $k \to 0$ and in the absence of a resonance, the coefficients a and b can be calculated from the elastic scattering T matrix, its derivative with respect to the energy, and the electric charge and magnetic dipole moment of the incident and outgoing particles, as detailed in the Appendix. The bremsstrahlung cross section is

$$\sigma = |M|^2\phi , \tag{3}$$

where ϕ is a phase-space factor which is given in the Appendix. Since the phase space is proportional to k, we can write

$$\phi = k\beta , \tag{4}$$

where β is a slowly varying function that cuts off at the limit of phase space. Substitution of Eqs. (2) and (4) in (3) yields

$$\sigma = \beta[\,|a|^2/k + (a^*b + ab^*) + (a^*c + c^*a + |b|^2)k + \cdots\,] \tag{5a}$$

$$\equiv \sigma_1/k + \sigma_2 + \sigma_3 k + \cdots , \tag{5b}$$

and we find that the bremsstrahlung cross section can also be expanded in a power series in k and that the first two terms in this series are calculable when $k \to 0$.

The statement that a and b in Eq. (5a) are calculable in the limit $k \to 0$ is called the Low theorem. The approximation of the radiative cross section by Eq. (5a) with the a and b coefficients calculated from Low's prescription and $c = 0$, we shall call the soft-photon approximation (SPA). Although the Low theorem applies only in the zero-photon-energy limit, it is of considerable interest to determine experimentally the extent to which the soft-photon approximation can be used to calculate radiative cross sections for photons of finite energy. Note that the coefficients of the powers of k in Eq. (5) are dependent on k, since the kinematics of the interacting particles depend on the four-momentum carried away by the

photon.

Figure 2 shows the results of using SPA to calculate the expected photon spectrum in $\pi^+ p \to \pi^+ p\gamma$ with incident pions of 300 MeV kinetic energy and for a particular geometry shown in the figure. The calculation is described in detail in the Appendix. We note that pion-nucleon scattering at this energy is dominated by the $\Delta(1236)$ resonance, whereas the derivation of the Low theorem assumes that no resonances are involved in the elastic scattering process.

Modern theories of the nucleon-nucleon interaction[5] are based on meson exchange. The relevant meson-nucleon scattering is by necessity always off the mass shell. But the known scattering amplitudes, such as for πN scattering, are all on-mass-shell amplitudes that must be modified before they can be applied to a quantitative nucleon-nucleon scattering calculation. Bremsstrahlung measurements provide a fine opportunity to investigate the off-mass-shell effects, as the photon is not a strongly interacting particle, and its coupling is too small to influence the πN scattering process. This is a distinct advantage over other reactions such as $pp \to pp\pi$.

The first stage of our program of studying πp bremsstrahlung, which we report here, was designed to study the magnetic dipole moment of the $\Delta^{++}(1236)$ resonance. The short lifetime of the Δ makes it impossible to employ the precession method for determining the magnetic dipole moment, and other ways must be used. Kondratyuk and Ponomarev[6] were the first to detail how a measurement of the photon spectrum in $\pi^+ p$ bremsstrahlung at the properly chosen geometry might

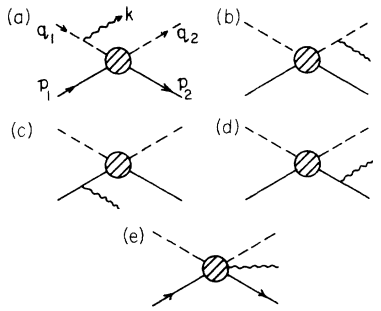

FIG. 1. Feynman diagrams for radiative pion-proton scattering: (a)–(d) "external" radiation; (e) "internal" radiation.

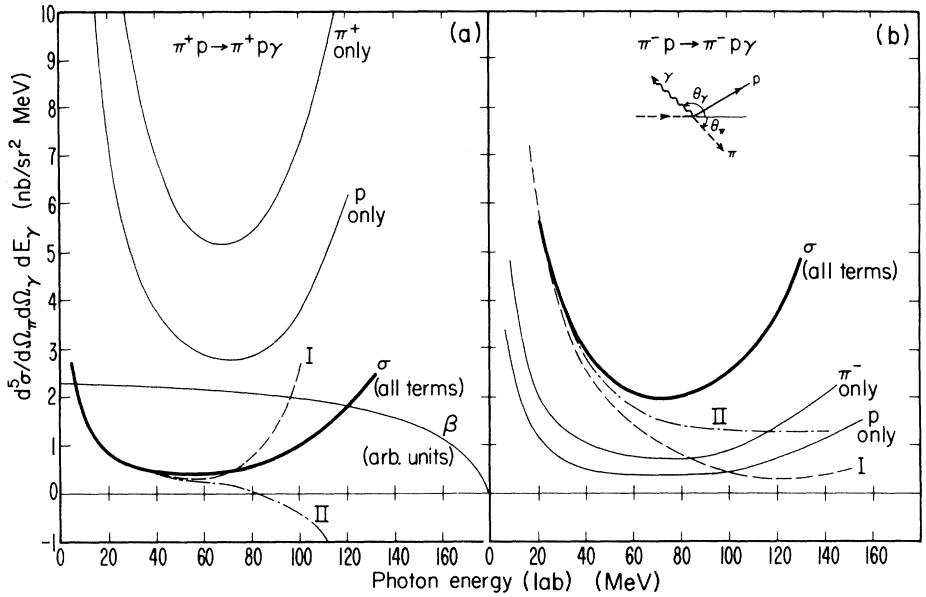

FIG. 2. Soft-photon-approximation calculation of the differential cross section in the lab system (heavy line) and several intermediate stages in the calculation. The curves labeled "π only" and "p only" include only the external radiation from the specified particles; those labeled "I" and "II" contain respectively the first term and the first and second terms of the expansion of Eq. (5b). The rise in cross section at high photon energy is due to a breakdown of the approximation; see the Appendix for details. β is the phase-space function described in the text; the present experiment has an acceptance which cuts off near $E_\gamma = 125$ MeV, well below the phase-space limit. The incident kinetic energy is 298 MeV and the geometry is that of counter G_4 of this experiment: $\theta_\pi = 50.5°$, $\theta_\gamma = -140°$, coplanar. (a) $\pi^+ p$ radiative scattering; (b) $\pi^- p$ radiative scattering.

reveal the magnetic dipole moment $\mu(\Delta^{++})$. The idea is that among the many Feynman diagrams symbolically represented by Fig. 1(e) is the one of Fig. 3(a), which represents the radiative decay of the Δ to itself, $\pi^+p \to \Delta^{++} \to \Delta^{++}\gamma \to \pi^+p\gamma$. This reaction is possible because of the finite mass width of the Δ. The dominant amplitude[7] is due to magnetic-dipole-moment radiation. This contribution can be observed most easily if the external radiation contributions of Figs. 1(a)–1(d) can be minimized. This can be accomplished by selecting photons that go backward with respect to the π^+ and proton; the external radiation amplitudes have maximum destructive interference in this configuration (see Fig. 2). The photon spectrum predicted by the model of Kondratyuk and Ponomarev, as amended by Vanzha and Musakhanov,[8] is given in Fig. 3(b). The value used for the dipole moment is $\mu(\Delta^{++}) = +2\mu(p)$, where $\mu(p)$ is the proton magnetic moment, as predicted by the quark model and SU(6).[9]

The process $\pi^-p \to \pi^-p\gamma$, measured under the same kinematic conditions as $\pi^+p \to \pi^+p\gamma$, should exhibit a quite different spectrum, since the interference between the π^- and p amplitudes is now constructive. Furthermore, the process of Fig. 3(a) should not contribute, since $\mu(\Delta^0)$ is predicted to be zero. Consequently, a measurement of both π^+p and π^-p bremsstrahlung provides a good test of the validity of the assumptions underlying the detailed calculations.

We have initiated a program of measurements of the processes $\pi^\pm p \to \pi^\pm p\gamma$. In the first stage, the incident pions have momentum 414 MeV/c (kinetic energy 298 MeV), corresponding to a πp center-of-mass energy of 1312 MeV. This energy is still sufficiently low that the $\Delta^{++}(1236)$ dominates the elastic π^+p cross section, yet high enough to see possible interesting structure effects such as that of internal radiation, in particular of magnetic-dipole-moment radiation of the $\Delta^{++}(1236)$. Preliminary results of this experiment have already been reported.[10,11] The present article contains the fully corrected results of the first stage of the investigation. The results obtained for other geometries and incident beam energies will be reported in later publications.

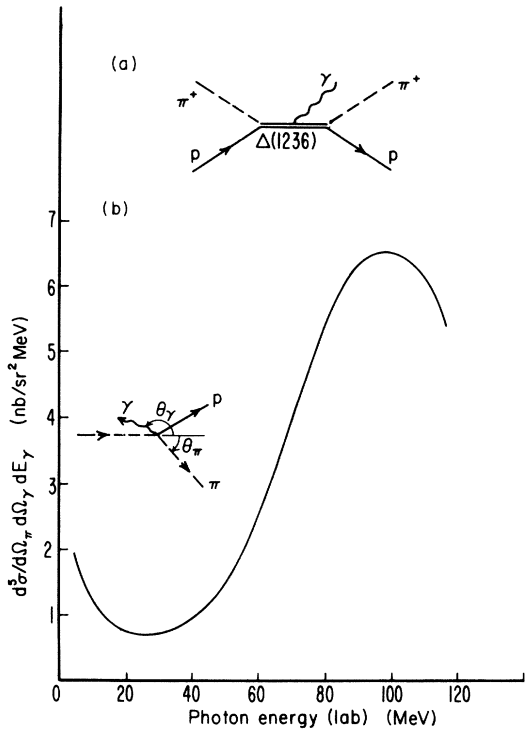

FIG. 3. (a) Feynman diagram for the contribution of radiation from the magnetic dipole moment of the $\Delta^{++}(1236)$. (b) Calculation of cross section in the model of Kondratyuk and Ponomarev, including the contribution of (a), at 298 MeV and for the geometry of counter G_1 in this experiment: coplanar, $\theta_\pi = 50.5°$, $\theta_\gamma = -160°$.

II. EXPERIMENTAL METHOD AND APPARATUS

The small expected cross section of $\pi p \to \pi p\gamma$ necessitated the design of a detector with a large acceptance. Furthermore, the measurement of such a small cross section was susceptible to background, which included (a) elastic scattering events with a random count in the photon detector; (b) "distorted" elastic events, in which rescattering or pion decay could simulate the radiative scattering kinematics; (c) π^0 production via the reaction $\pi^\pm p \to \pi^\pm p\pi^0$; and (d) beam interactions in the target walls. The separation of signal from background events was done with a 2-constraint fit that made use of the following measured variables: (i) the incident pion momentum and direction, (ii) the scattered pion momentum and direction, (iii) the proton direction, and (iv) the photon direction. The apparatus consisted of a wide-aperture magnetic spectrometer with wire spark chambers to detect the scattered pion, a system of wire spark chambers and a scintillator range telescope for the proton, and a set of lead-glass Cherenkov counters for the photon. Accurate time-of-flight information from each detector facilitated particle identification and provided good discrimination against random coincidences in the photon counters.

The experimental setup is shown in Figs. 4 and 5, and the location of the various detectors is summarized in Table I. The scattering angles have been defined for convenience in describing and surveying the apparatus: α is measured

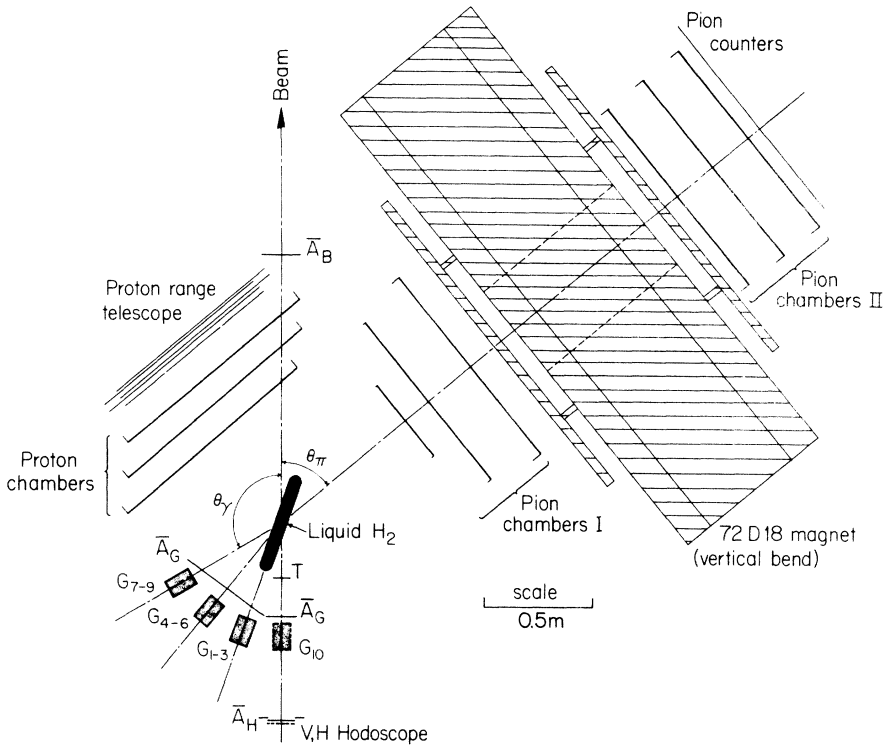

FIG. 4. Experimental apparatus. G_1 through G_{10} are the lead-glass photon counters, of which only G_1, G_4, and G_7 lie in the horizontal plane. Dimensions are given in Table I.

clockwise from the beam line in the horizontal plane and β is the angle of elevation measured upward from the horizontal plane. They are related to the more conventional scattering angles θ (scattering angle measured from the beam line) and ϕ (azimuthal angle about the beam line) by the conversion formulas

$$\cos\theta = \cos\alpha\cos\beta\,, \quad \tan\phi = \tan\beta\csc\alpha\,.$$

A. Beam

The pions were produced at 0° in the external proton beam of the Lawrence Berkeley Laboratory 184-in. synchrocyclotron. The length of the production target (48 cm of CH_2 for the π^+ runs, 15 cm of beryllium for π^-) was chosen for maximum pion rate; the π^+ production was dominated by the two-body reaction $pp \to d\pi^+$. The two-bend, intermediate-focus pion beam included three quadrupole doublets and one singlet. A 5.5-cm CH_2 degrader was placed at the first focus of the π^+ beam to remove protons from the beam. The beam spot size was approximately 6.3×6.3 cm [FWHM (full width at half maximum)] at the hydrogen target. The important beam parameters are listed in Table II.

B. Hydrogen target

The liquid hydrogen target was a flat flask 5.2 ± 0.1 cm wide with 0.13-mm Mylar walls, inclined at an angle of 20.5 ± 0.5 degrees to the beam line in order to minimize the energy loss of recoil

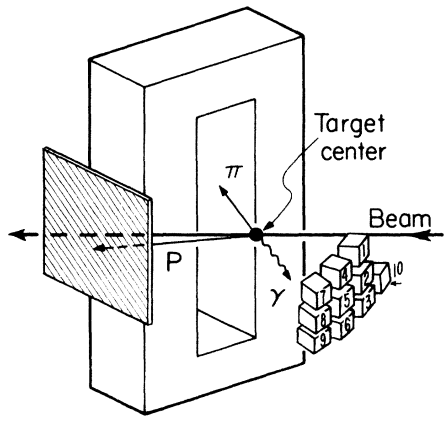

FIG. 5. Schematic perspective view of the experimental apparatus (not to scale). The pion detection arm is represented by the magnet yoke, and the proton arm by a plane of scintillation counters. For dimensions and details, see Fig. 4 and Table I.

TABLE I. Position of particle detectors.

	Horiz. angle α [a]	Vert. angle β [a]	Distance from H_2 target center
pion	$50.5° \pm 7.0°$ [b]	$0°^{+24°}_{-10°}$ [b]	73.8 cm [c]
proton	−10.6° to 63.2°	−26.4° to 26.4°	92.1 cm [d]
photon [e]			
G_1	−160.0°	0°	61.1 cm
G_2	−160.0°	−18.0°	56.0 cm
G_3	−160.0°	−36.0°	56.0 cm
G_4	−140.0°	0°	56.0 cm
G_5	−140.0°	−18.0°	56.0 cm
G_6	−140.0°	−36.0°	56.0 cm
G_7	−120.0°	0°	56.0 cm
G_8	−120.0°	−18.0°	56.0 cm
G_9	−120.0°	−36.0°	56.0 cm
G_{10}	180.0°	−36.0°	56.0 cm

[a] Angles defined in text.
[b] Approximate angular acceptance for scattered momentum 340 MeV/c.
[c] Distance to first pion spark chamber.
[d] Distance to first plane of counters.
[e] Angles and distances measured to center of front face of 10.2×10.4×15.2-cm counter.

protons leaving the target. The average length of hydrogen traversed by the beam was therefore 14.5 ± 0.4 cm. The liquid hydrogen was in equilibrium with the gas in a closed system whose pressure was slightly above 1 atmosphere. The target flask was surrounded by a gas ballast flask with 0.25-mm Mylar walls, and by 20 layers of 0.006-mm aluminized Mylar superinsulation for heat shielding. The vacuum chamber surrounding the gas ballast was a 17.8-cm diameter aluminum cylinder with 0.81-mm walls.

C. Pion detector

The pion spectrometer is shown in Fig. 4. The magnet was a picture-frame dipole with an aperture of 183 cm by 46 cm and a 46-cm gap between the pole faces. The magnet was oriented with the main component of magnetic field horizontal, so as to deflect the particles vertically downward. Iron plates of 5.7 cm thickness were attached to both faces of the magnet to reduce the fringe field in the region of the spark chambers.

The trajectory of the scattered pion before the magnet was determined by three wire spark chambers of dimensions 50×75 cm, 75×75 cm, and 100×100 cm, with magnetostrictive readout. The trajectory after the magnet was determined by three 1×2-m magnetostrictive spark chambers. Four contiguous 63×46×1.3-cm scintillation counters, $\pi_1 - \pi_4$, were mounted behind the last spark chamber and were used for triggering and time-of-flight measurements. The solid angle acceptance for pions was approximately 120 msr over almost the entire momentum range.

TABLE II. Parameters of pion beam.

Particle	Lab momentum [a,b] (MeV/c)	Kinetic energy [a] (MeV)	Momentum spread	Muon/pion ratio [d]	$e^{\pm}$/beam ratio [e]	Average rate (sec^{-1})
π^+	414 ± 3	298 ± 3	±2.6%	4.0 ± 1.5%	0.5 ± 0.5%	8×10^5
π^-	414 ± 3	298 ± 3	±2.6%	4.0 ± 1.5%	7.4 ± 1.0%	1×10^5

[a] At center of liquid H_2 target.
[b] Determined from range in copper, corrected for multiple scattering.
[c] Deduced from width of differential range curve, including straggling.
[d] Calculated and measured from differential range curve.
[e] Measured with Freon threshold Cherenkov counter.

D. Proton detector

The proton detector consisted of three 1×1-m wire spark chambers with magnetostrictive readout, followed by a range telescope consisting of 13 scintillation counters (P_1–P_{13}) arranged to form 6 planes, 91×91 cm^2. Only the first plane of counters, consisting of P_1–P_3, was required in the trigger; the counters in the other planes triggered electronic "latches" which were read by the on-line computer. Behind the second and subsequent planes were copper absorbers of varying thickness chosen to provide a resolution of ±8 to ±10 MeV in proton energy. The first plane absorbed protons up to 35 MeV and the fifth plane up to 115 MeV. The discriminators for the first five planes were set to trigger on proton pulse heights above three times minimum ionization, corresponding to the highest-energy protons to be detected, while the last plane was set for minimum ionizing particles and was used to reject pions in the proton arm.

The proton detector subtended a solid angle of approximately 1 sr, and did not restrict the experimental acceptance at most photon energies. Protons from elastic scattering and soft-photon radiative events were detected near the outer edge of the proton counters, while hard-photon radiative events produced protons at smaller angles relative to the beam. In order to detect protons at small angles, we let the pion beam pass through the proton spark chambers near one edge. The region of each chamber traversed by the beam was electrically disabled.

E. Photon detector

The photon detector consisted of ten separate counters, G_1–G_{10}, which were arranged in three rows and four columns (see Figs. 4 and 5 and Table I). Each counter consisted of a block of Bourns PEMG2 lead glass, 10×10 cm in area and 15 cm (4.7 radiation lengths) thick. The lead glass was connected by a 13-cm thick ultraviolet-transmitting Plexiglas light pipe to an RCA 4522 photomultiplier tube with a 11.5-cm diameter photocathode. Optical grease was used at the couplings. To increase the efficiency for detecting Cherenkov light near the edges and thus reduce edge effects, the lead glass was jacketed by a box of 0.6-cm Plexiglas which was also connected at one end to the light pipe.

The photon counters provided spatial and timing information. The photon energy was calculated from the photon angle and the charged-particle information. Thus only the efficiency and solid angle of the photon counters were important. All counters were calibrated with 25-MeV positrons obtained by suitable modification of our beam line, and the gain was routinely checked with 3.5-MeV β radiation from a ^{106}Ru source. Two counters were also tested in an electron beam where we measured the efficiency for detecting electrons of 9, 10, 12, 16, and 25 MeV at the normal operating voltages.[12] The efficiency for electrons above 16 MeV is (98±2)%. These electron efficiency results were used to calculate the photon detection efficiency in a Monte Carlo program. For a photon which enters along the counter axis, the efficiency is (81±5)% at E_γ = 20 MeV and (92±2)% for E_γ = 50 MeV. The product of solid angle and efficiency (Fig. 6) is found by integrating over the target region and correcting for interactions in the Plexiglas and attenuation of light. Details of the construction and calibration of the photon detectors are given in Ref. 12.

F. Other counters

The incident beam was defined at the exit of the last quadrupole magnet by four vertical counters, V_1–V_4, each 1.9 cm wide, and by six horizontal counters, H_1–H_6, each 2.5 cm wide. The beam was further defined, just before the hydrogen target, by a 7.6×7.6×0.64-cm counter T which was also used for timing.

An anticounter A_H, with a central hole surround-

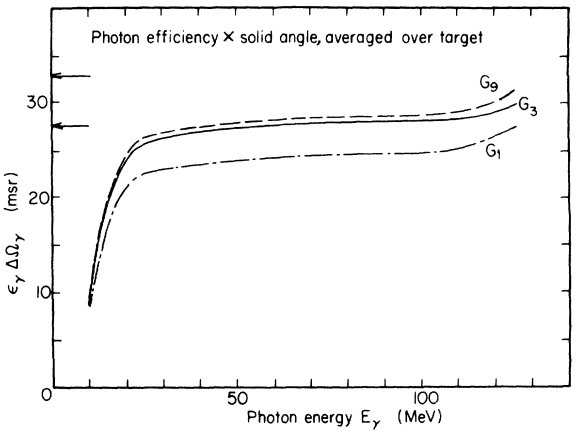

FIG. 6. Product of efficiency and solid angle for the lead-glass photon counters, averaged over the target region and experimental acceptances. The face of counter G_1 subtends a solid angle of 27.6 msr at the center of the target; counters G_2–G_{10} are subtend 32.8 msr (represented by the two arrows on the vertical axis). The curves for counters G_2–G_{10} lie within the region bounded by G_3 and G_9. The increase above 110 MeV is due to a shift in the distribution of accepted interaction points in the target as the pion and proton acceptances begin to cut off.

ing the beam hodoscope, reduced accidental counts due to the beam halo. Downstream of the target was a beam anticounter A_B, which helped to eliminate multiple pions in the beam. This counter was latched, rather than cabled in anticoincidence, in order to allow its effects to be examined more closely. The photon counters were guarded by anticounters A_G, which rejected charge particles both from the target and from elsewhere along the beam line.

G. Electronics

An incident pion was defined by the coincidence

$$\pi_{\text{in}} = V_i H_j T C \overline{A}_H (\overline{V}_m + \overline{H}_m) .$$

C is a fast timing signal generated by the cyclotron RF system. It was used to reduce non-beam-related accidentals. $(\overline{V}_m + \overline{H}_m)$ represents the triggering of two vertical or horizontal beam hodoscope counters, indicating a beam double. T is a signal from the differential discriminator of counter T which was set to reject pulses with pulse height greater than 1.5 times minimum ionization. An event trigger was defined by

$$E = \pi_{\text{in}} G \pi P \overline{A}_G ,$$

where G, π, and P represent logical "or" signals from the photon, pion, and proton counters, respectively.

H. Data collection

An on-line Digital Equipment Corporation PDP-8/I computer handled all relevant data for each event: information from the 3 sets of wire spark chambers, all counters, and the time-of-flight of the proton, pion, and photon. Distributions of all quantities were accumulated for visual display, and the raw data were written on magnetic tape for off-line analysis. The π^+ trigger rate was approximately 0.27 per 10^6 beam pions and the π^- trigger rate approximately 0.04 per 10^6 beam pions. The difference was mainly due to the difference in π^+ and π^- beam rates. The event triggers consisted primarily of accidental coincidences, as will be shown in Sec. III.

Interspersed among the data runs were additional runs with the target flask empty, as well as "elastic" runs in which the photon was eliminated from the trigger requirements.

III. ANALYSIS

A. Kinematic reconstruction

The analysis of the π^+ and π^- data followed the same sequence of steps. The numbers quoted below apply to the π^+ data.

(1) The first step of the analysis consisted of constructing from the spark chamber information three independent straight line trajectories: one pion track before the magnet, one pion track after the magnet, and one proton track. For every trajectory we required sparks in at least two of the three chambers in the set. Approximately 14% of the triggers were rejected for insufficient chamber information, with 2% attributed to bad triggers without a real track and the remainder to chamber inefficiencies.

(2) All reconstructed events for which the distance of closest approach of the pion and proton track, D_p, was greater than 3.8 cm were considered uncorrelated and not analyzed further. This constituted a 3-standard-deviation cut in D_p. In addition, the point of intersection of the two tracks was required to lie within the region of the hydrogen target flask. These cuts eliminated 32% of the total triggers, including most of the contribution of the target vacuum-chamber walls.

(3) The pion tracks before and after the magnet were tested for similar orientation angle $\alpha_{1,2}$ in the nondispersive plane after correction for focusing effects, and the distance of closest approach D_α was determined. A cut of 1° on $\alpha_1 - \alpha_2$ and 1.8 cm on D_α was imposed to reject events in which the pion had decayed or scattered from a magnet pole face. This cut removed 15% of the triggers.

(4) Other reasons for event rejection were multiple beam hodoscope latches (13% of the triggers), multiple photon latches (1.3%), pions in the proton detector (negligible), and protons in the pion detector (6.8%). The rejection of the last category was done on the basis of the pion time of flight. The multiple beam hodoscope latches were the consequence of a small inefficiency in our method for rejecting beam doubles.

(5) The momentum of the scattered pion was calculated from the pion trajectories before and after the magnet, using a five-variable polynomial expression whose coefficients were evaluated by computer ray-tracing through the measured magnetic field.

(6) Each event that passed the above restrictions was subjected to a 2-constraint least-squares fit to the hypothesis $\pi p \to \pi p \gamma$ using the measured values of the direction and energy of the incident and scattered pion and the directions of the proton and photon. The fitting procedure minimized a χ^2-like variable constructed from the measured quantities weighted according to their estimated errors. The photon energy and proton energy were calculated from the best fit. Elastic scattering events with a random count in a photon counter satisfy the radiative scattering kinematics

with $E_\gamma = 0$ and yield a good value of χ^2. Figure 7 shows the distribution of calculated photon energy for all events. The large peak consists almost entirely of elastic events which reconstruct with $E_\gamma = 0 \pm 3.5$ MeV. The good resolution in E_γ allows us to eliminate nearly all the elastic events by applying the energy cut $E_\gamma \geq 20$ MeV. Events with E_γ between 15 and 20 MeV were not discarded, but were reexamined after subsequent cuts.

(7) Next we applied a cut of ± 3 nsec on the photon time-of-flight (TOF); the electronic logic had accepted photons within a ± 13-nsec gate. Above 20 MeV, the photon peak stands clearly above a small background. For lower photon energies, the signal-to-background ratio deteriorates rapidly, reaching 1:1 for $10 \leq E_\gamma < 15$ MeV. Events with photon TOF within 3 nsec of the accepted peak were also retained in the analysis, so that correction for the random background under the peak could subsequently be made.

(8) The proton range was used to calculate the missing mass of the neutral particle in a 0-constraint fit which made no use of the photon counter information. The resulting missing-mass distribution is shown in Fig. 8, where a clear separation is seen between radiative events ($m_X^2 \approx 0$) and events of the reaction $\pi^+ p \to \pi^+ p \pi^0$ [$m_X^2 \approx (140\ \text{MeV})^2$]. A cut was applied at $|m_X^2| < (84\ \text{MeV})^2$. This cut eliminated nearly all of the tail from the χ^2 distribution.

(9) The surviving events were corrected for random background in the photon TOF. For each energy bin, the TOF distribution consisted of a narrow peak superposed on a nearly flat background (Fig. 9). The number of true events for each photon energy bin and photon counter was calculated by subtracting from the "peak" the number of events contained in an interval of equal width outside the peak. For the final cut at $\chi^2 < 15$, these corrections averaged 21% for $15 < E_\gamma < 20$ MeV, 9% for $20 < E_\gamma < 30$ MeV, and less than 2% for $E_\gamma > 30$ MeV.

(10) After the random TOF background was subtracted, the χ^2 distribution was cut at $\chi^2 = 15$. In each region of photon energy, the χ^2 distribution (Fig. 10) consisted of a sharp peak with $\chi^2 < 5$, falling rapidly to a small and nearly flat distribution beyond $\chi^2 = 25$. Since the number of "excess" events between $\chi^2 = 15$ and 25 is nearly equal to the extrapolation of the flat background under $\chi^2 < 15$, it was decided that a cut at $\chi^2 < 15$ with no χ^2 background subtraction was a reasonable choice. The error associated with this event selection was estimated at $\pm 7.5\%$ for $E_\gamma < 40$ MeV, falling to $\pm 1.5\%$ for $E_\gamma > 100$ MeV, well within the statistical accuracy in each energy bin.

The only important difference in the analysis of the π^- data is that the photon TOF cut is not significant since the low π^- beam rate and small $\pi^- p$ elastic cross section resulted in a negligible back-

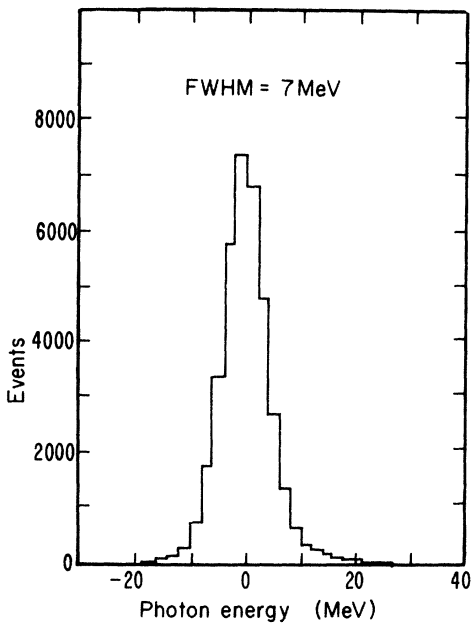

FIG. 7. Distribution of reconstructed photon energies for all events. The peak centered at 0 is due predominantly to elastic scattering events ($E_\gamma = 0$) detected in coincidence with a random trigger in a photon counter; the width of the peak thus indicates the experimental resolution in photon energy.

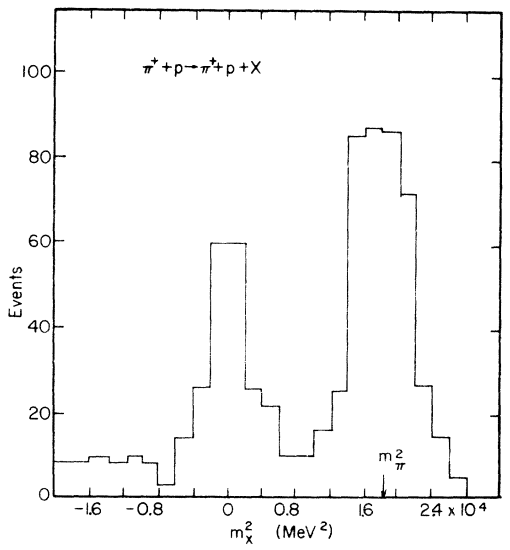

FIG. 8. Distribution of missing mass of the neutral particle under the hypothesis $\pi^+ p \to \pi^+ p x^0$. The two peaks at 0 and $(135\ \text{MeV})^2$ correspond to radiative scattering and π^0 production, respectively.

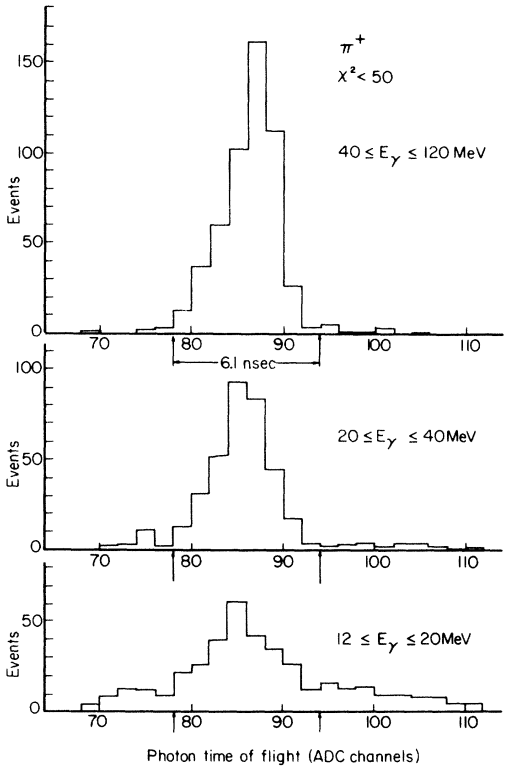

FIG. 9. Distribution of time of flight in photon counters after the missing-mass cut. One channel = 0.38 nsec. The events outside the peak are due to random background.

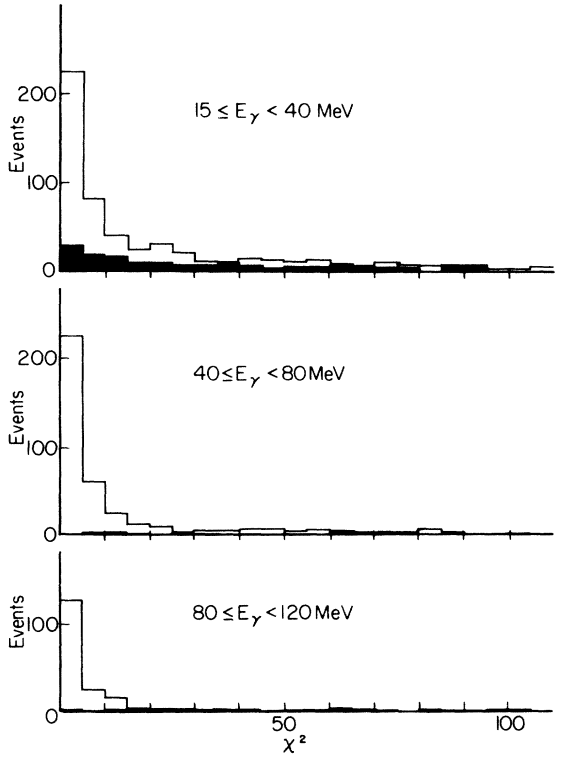

FIG. 10. Distribution of pseudo-χ^2 variable for events passing all other cuts. The open histogram represents the events contained within a photon TOF window of ±3 nsec; the solid histogram contains out-of-time "background" events whose TOF is within 3 nsec of the accepted window.

ground of random photon triggers. Thus the ratio of good radiative events to triggers was much higher for the π^- than for the π^+ data (7% and 0.25%, respectively).

Table III presents the number of good events for each photon counter and energy bin for the two sets of data. Empty-target runs yielded a negligible rate of accepted events, so that no empty-target subtraction was necessary.

B. Cross-section calculation

The differential cross section in the laboratory system for $\pi^\pm p \to \pi^\pm p\gamma$ was calculated for each photon counter i and each interval of photon energy as

$$d\sigma_i(E_\gamma) \equiv \frac{d^5\sigma_n}{d\Omega_\pi\, d\Omega_\gamma\, dE_\gamma} = \frac{Y}{BT\Delta E_\gamma (\Delta\Omega_\pi g_p)_i (\Delta\Omega_\gamma \epsilon_\gamma)_i \epsilon_{sc}\epsilon_c\epsilon_{surv}} .$$

Y = number of events with photon energy between $E_\gamma - \frac{1}{2}\Delta E_\gamma$ and $E_\gamma + \frac{1}{2}\Delta E_\gamma$, corrected for small random TOF background.

B = number of incident pions, given by the number of recorded beam coincidences, N_{beam} corrected for: η_e, η_μ = fractional electron and muon contaminations (Table II); η_{mult} = fraction of recorded beam particles associated with an extra particle within resolving time, causing rejection by the analysis program; η_{att} = attenuation of beam by interactions in hydrogen and target walls; η_{anti} = fraction of good events rejected by random coincidences with anticounters; $\eta_{\gamma d}$ = fraction of good events rejected because more than one photon counter was latched.

T = number of protons per unit area transverse to beam in hydrogen target as described in Sec. II B; $T = (6.07 \pm 0.19) \times 10^{23}$ cm^{-2}.

ΔE_γ = width of photon energy interval.

$(\Delta\Omega_\pi g_p)_i$ = effective solid angle acceptance for pions, corrected for the geometric acceptance of protons, calculated by Monte Carlo simulation of events (Fig. 11). The pion solid angle is nearly independent of photon energy. The proton acceptance factor is essentially unity from 20 to 100 MeV photon energy, falling to 0.96 at 15 MeV and to between 0.97 and 0.48 (for different photon

TABLE III. (a) Number of good $\pi^+p \to \pi^+p\gamma$ events, distributed according to laboratory photon energy and photon counter. Random time-of-flight background has been subtracted, increasing the statistical errors which are otherwise taken as the square root of the number of events. (b) Number of good $\pi^-p \to \pi^-p\gamma$ events, distributed according to laboratory photon energy and photon counter. No time-of-flight background subtraction was necessary.

(a)

Photon energy (MeV)	Photon counter number 1	2	3	4	5	6	7	8	9	10	All
15–20	1	3	12	1	5	9	8	10	11	13	73
20–30	9	8	16	7	2	9	12	13	27	27	130
30–40	7	9	11	5	9	6	11	9	16	22	105
40–50	7	5	15	10	7	9	3	7	12	11	86
50–60	7	9	8	4	1	4	9	10	15	5	72
60–70	4	5	7	6	9	5	8	10	15	11	80
70–80	7	2	6	1	5	6	7	5	11	15	65
80–90	5	5	4	3	5	4	4	3	18	5	56
90–100	1	2	7	7	3	6	4	4	6	2	42
100–110	3	3	7	3	2	2	6	3	3	2	34
110–120	1	3	1	1	1	3	1	2	2	2	17

(b)

Photon energy (MeV)	Photon counter number 1	2	3	4	5	6	7	8	9	10	All
15–30	2	2	2	4	2	1	3	3	4	4	27
30–50	3	5	4	4	2	1	1	2	9	3	34
50–70	1	2	0	2	1	2	3	2	2	3	18
70–90	1	2	2	2	1	1	1	1	1	3	15
90–120	2	1	0	0	1	0	1	3	2	0	10

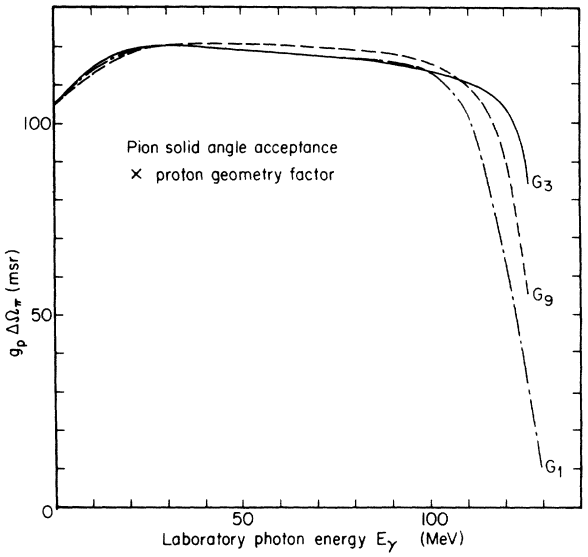

FIG. 11. Product of solid angle acceptance for pions and geometrical acceptance efficiency for protons averaged over all target positions. The function was calculated separately for each photon counter by a Monte Carlo method; typical curves are shown.

counters) at 115 MeV.

$(\Delta\Omega_\gamma \epsilon_\gamma)_i$ = average solid angle and efficiency of photon counter, described in Sec. II*E*, and shown in Fig. 6.

ϵ_{sc} = spark chamber efficiency, calculated for individual runs from the relative numbers of 2- and 3-spark fits for each set of 3 chambers. Consistent results for ϵ_{sc} were obtained using (a) the final sample of radiative scattering events, and (b) the elastic scattering events which constituted the majority of the triggers. Most of the inefficiency was due to the pion chambers; the protons, which were at least 3 times minimum ionizing, were detected with an inefficiency of less than 2%.

ϵ_c = efficiency of scintillation counters, measured in separate tests.

ϵ_{surv} = survival probability of outgoing particles $= (1-\eta_\gamma)(1-\eta_\pi)(1-\eta_p)(1-\eta_d)$, where η_γ = interactions of photon in the target and in the photon veto counters; η_π = interactions of pions in the target, chambers, and air path; η_p = interactions of multiple scattering of protons in the target and chambers; η_d = probability of losing an event by pion decay, estimated by a Monte Carlo calculation.

Numerical values for the cross section factors and corrections are given in Table IV.

We have divided the events into 10-MeV-wide intervals of photon energy, except for a single 5-MeV-wide bin from 15 to 20 MeV. Although the variation in cross section over the bin width is considerable in the low-energy bins, the error due to averaging the cross section over the finite energy interval is always less than 1.5% and has been ignored. Table V gives the cross section in the laboratory system for each photon counter and interval of photon energy. Figure 12 gives the Jacobian factor $J = (d\Omega_\pi^* d\Omega_\gamma^* dE_\gamma^*)/(d\Omega_\pi\, d\Omega_\gamma dE_\gamma)$, which can be used to convert the cross section to the center-of-mass system (CMS).

IV. RESULTS

A. Comparison of data with theory

The small number of events in each photon counter and photon energy interval necessitates combining the data to exhibit the prominent features of the cross section. The photon energy dependence can best be shown by averaging the differential cross section over all 10 photon counters, weighted by their geometrical solid angles. Even when the data are combined in this way, the errors are

TABLE IV. Normalization factors and corrections used in cross-section calculation. The symbols are defined in the text; those designated by ϵ are absolute efficiency factors which multiply the number of beam particles, while the η's are percent corrections, all of which reduce the effective number of beam particles.

Factor or correction	π^+	π^-
N_{beam}	8.43×10^{11}	3.83×10^{10}
ϵ_{sc}	0.86 ± 0.02	0.72 ± 0.04
ϵ_c	0.98 ± 0.01	0.98 ± 0.01
η_{mult}	$(2.2\pm1.0)\%$	$(0.4\pm0.2)\%$
η_{att}	$(4.1\pm0.4)\%$	$(3.0\pm0.3)\%$
η_{anti}	$(7.7\pm1.7)\%$	$(1.3\pm0.6)\%$
$\eta_{\gamma d}$	$(1.3\pm0.5)\%$	$(0.2\pm0.1)\%$
η_γ	2.5% to 6.6%	2.5% to 6.6%
η_π	4.8% to 7.5%	2.9% to 4.2%
η_p	2.1% to 2.4%	2.1% to 2.4%
η_d	$(12.2\pm2.0)\%$ to $(17.4\pm5.1)\%$	$(12.2\pm2.0)\%$ to $(17.4\pm5.1)\%$

TABLE V. (a) $\pi^+p\to\pi^+p\gamma$ laboratory differential cross section measured for individual photon counters. The last column gives the average over 10 counters, weighted by solid angle. The errors are predominantly statistical. The statistical error is taken as the square root of the number of events, and is increased when random background is subtracted. (b) Laboratory differential cross section for $\pi^-p\to\pi^-p\gamma$.

(a)

Photon energy (MeV)	Laboratory differential cross section (nb/sr^2 MeV) for photon counter number 1	2	3	4	5	6	7	8	9	10	Avg.
15–20	0.3 ± 0.7	0.9 ± 0.9	3.5 ± 1.2	0.3 ± 0.5	1.4 ± 0.8	2.6 ± 1.0	2.2 ± 0.9	2.7 ± 1.2	3.1 ± 1.3	3.6 ± 1.1	2.09 ± 0.37
20–30	1.2 ± 0.5	0.9 ± 0.4	1.9 ± 0.6	0.8 ± 0.3	0.2 ± 0.4	1.1 ± 0.4	1.4 ± 0.4	1.5 ± 0.4	3.1 ± 0.7	3.1 ± 0.7	1.54 ± 0.21
30–40	0.9 ± 0.4	1.0 ± 0.4	1.3 ± 0.4	0.6 ± 0.3	1.0 ± 0.4	0.7 ± 0.3	1.2 ± 0.4	1.0 ± 0.3	1.8 ± 0.5	2.4 ± 0.6	1.20 ± 0.16
40–50	0.9 ± 0.4	0.6 ± 0.3	1.7 ± 0.5	1.1 ± 0.4	0.8 ± 0.3	1.0 ± 0.4	0.3 ± 0.2	0.8 ± 0.3	1.3 ± 0.5	1.2 ± 0.4	0.98 ± 0.13
50–60	0.9 ± 0.4	1.0 ± 0.3	0.9 ± 0.3	0.5 ± 0.2	0.1 ± 0.1	0.5 ± 0.3	1.0 ± 0.3	1.1 ± 0.4	1.6 ± 0.4	0.6 ± 0.3	0.82 ± 0.11
60–70	0.5 ± 0.3	0.6 ± 0.3	0.8 ± 0.3	0.7 ± 0.3	1.0 ± 0.3	0.6 ± 0.3	0.9 ± 0.3	1.1 ± 0.3	1.6 ± 0.4	1.2 ± 0.4	0.91 ± 0.12
70–80	0.9 ± 0.4	0.2 ± 0.2	0.7 ± 0.3	0.1 ± 0.1	0.6 ± 0.3	0.7 ± 0.3	0.8 ± 0.3	0.5 ± 0.2	1.2 ± 0.4	1.7 ± 0.4	0.73 ± 0.10
80–90	0.7 ± 0.3	0.6 ± 0.3	0.5 ± 0.3	0.3 ± 0.2	0.6 ± 0.3	0.5 ± 0.2	0.4 ± 0.2	0.3 ± 0.2	1.9 ± 0.5	0.6 ± 0.3	0.64 ± 0.09
90–100	0.1 ± 0.1	0.2 ± 0.2	0.8 ± 0.3	0.8 ± 0.3	0.3 ± 0.2	0.7 ± 0.3	0.5 ± 0.2	0.4 ± 0.2	0.7 ± 0.3	0.2 ± 0.2	0.49 ± 0.08
100–110	0.4 ± 0.2	0.4 ± 0.2	0.8 ± 0.3	0.4 ± 0.2	0.2 ± 0.2	0.2 ± 0.2	0.7 ± 0.3	0.3 ± 0.2	0.3 ± 0.2	0.2 ± 0.2	0.41 ± 0.08
110–120	0.2 ± 0.2	0.4 ± 0.2	0.1 ± 0.1	0.2 ± 0.2	0.2 ± 0.2	0.4 ± 0.2	0.2 ± 0.2	0.3 ± 0.2	0.2 ± 0.2	0.2 ± 0.2	0.24 ± 0.06

(b)

Photon energy (MeV)	Laboratory differential cross section (nb/sr^2 MeV) for photon counter number 1	2	3	4	5	6	7	8	9	10	Combined
15–30	5.0 ± 3.6	4.3 ± 3.0	4.4 ± 3.2	8.6 ± 4.4	4.2 ± 3.0	2.2 ± 2.2	6.5 ± 3.7	6.2 ± 3.6	8.4 ± 4.3	8.3 ± 4.3	5.8 ± 1.3
30–50	4.9 ± 2.9	7.0 ± 3.2	5.7 ± 2.9	5.6 ± 2.8	2.8 ± 2.0	1.4 ± 1.4	1.4 ± 1.4	2.7 ± 1.9	12.0 ± 4.3	4.1 ± 2.4	4.8 ± 0.9
50–70	1.6 ± 1.6	2.8 ± 2.0	0.0 ± 1.4	2.8 ± 2.0	1.4 ± 1.4	2.8 ± 2.0	4.1 ± 2.4	2.7 ± 1.9	2.7 ± 1.9	4.1 ± 2.4	2.5 ± 0.6
70–90	1.6 ± 1.6	2.8 ± 2.0	2.8 ± 2.0	2.8 ± 2.0	1.4 ± 1.4	1.4 ± 1.4	1.4 ± 1.4	1.3 ± 1.3	1.3 ± 1.3	4.1 ± 2.4	2.1 ± 0.6
90–110	3.4 ± 2.4	1.5 ± 1.5	0.0 ± 1.5	0.0 ± 1.5	1.5 ± 1.5	0.0 ± 1.5	0.0 ± 1.5	2.8 ± 2.0	2.7 ± 1.9	0.0 ± 1.4	1.1 ± 0.4

predominantly statistical. The energy-dependent systematic errors are estimated at between 3% and 9% in addition to a "normalization" error, independent of photon energy, which is ±4.8% for the π^+ and ±6.8% for the π^- data.

The cross sections are shown in Fig. 13, where they are compared with averaged theoretical cross sections calculated from the soft-photon approximation and the models of Kondratyuk and Ponomarev[6,8] and Fischer and Minkowski,[13,14] to be discussed later. While the cross sections agree with theory in the soft-photon region, there is a large discrepancy in the region where the Δ(1236) should manifest itself in the final state. (It should be noted that the prediction of enhanced cross sections at higher photon energies does not depend on the existence of the Δ magnetic-moment contribution, but simply on the resonant amplitude in the π-p system.)

Even in the restricted region of photon angles

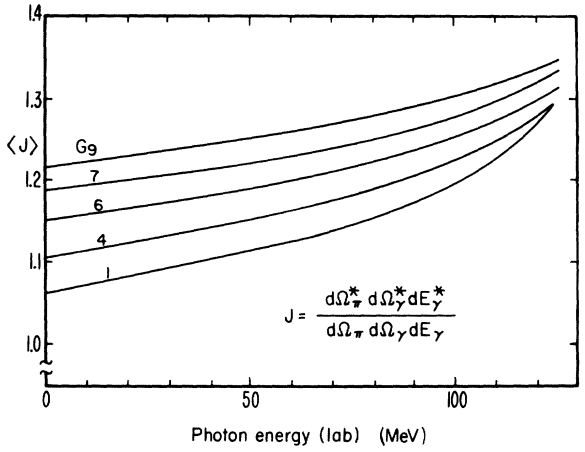

FIG. 12. Jacobian transformation factor for converting differential cross section from lab to CMS variables, averaged over the acceptance for each photon counter. Typical curves are shown.

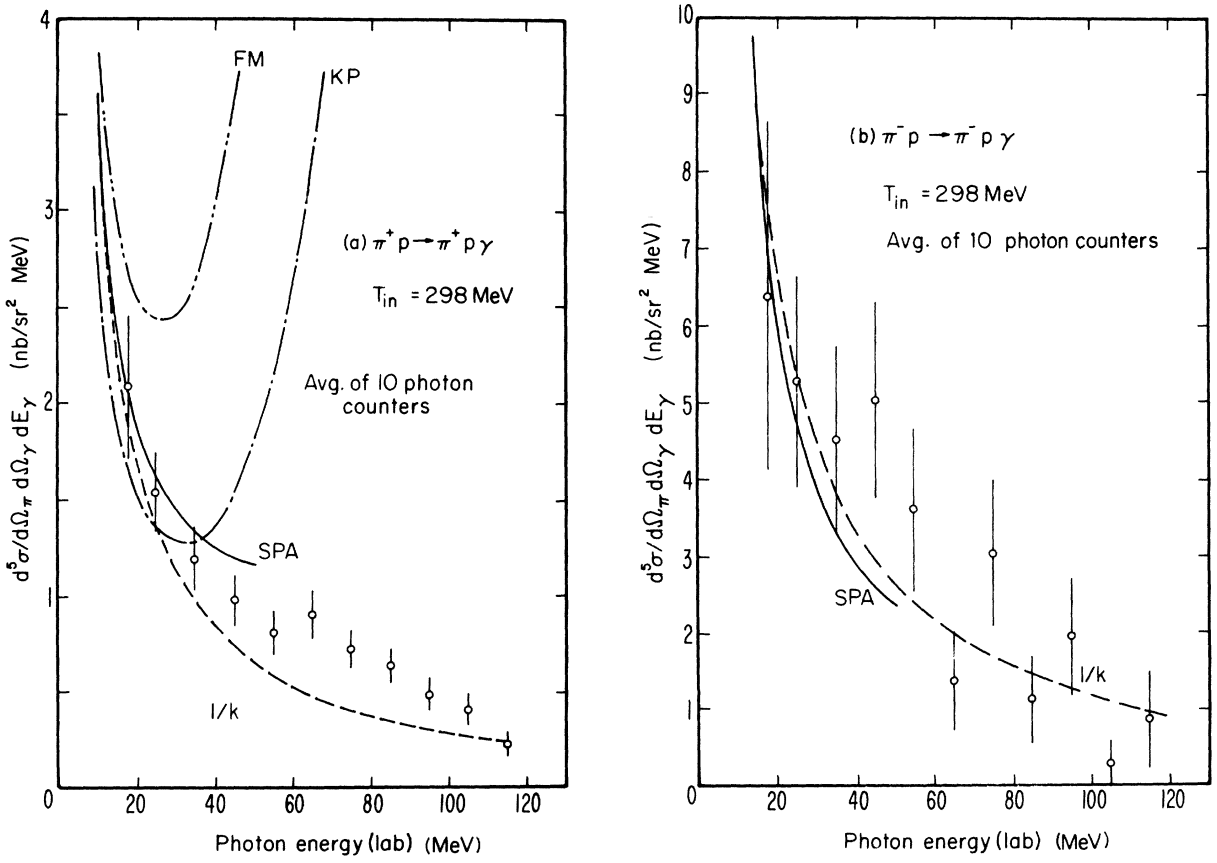

FIG. 13. Differential cross section in the laboratory, averaged over all 10 photon detectors, for (a) $\pi^+ p$ and (b) $\pi^- p$ radiative scattering. The theoretical curves are described in the text: SPA = soft-photon approximation; KP = Kondratyuk and Ponomarev (corrected by Vanzha and Musakhanov); FM = Fischer and Minkowski. The experimental acceptance cuts off near E_γ = 125 MeV.

covered by the 10 photon detectors, the SPA predicts π^+ cross sections which differ considerably among the individual counters (Fig. 14). This counter-to-counter variation is understandable in view of the strongly direction-dependent factors appearing in the SPA calculation (see the Appendix). (The counter-to-counter variations in the π^- cross section are less pronounced since the constructive interference in this case is not as dramatic.) The experimental variation of cross section among the 10 photon counters is seen in Table VI, where we present the number of events in each counter, compared to SPA predictions integrated over acceptance.

One problem in comparing experimental and theoretical cross sections in our geometry is that the pion spectrometer subtends a large solid angle (approximately 130 msr) and thus the averaging of the cross section over the geometrical acceptance involves integration over a wide variation in true differential cross section, owing to the rapid angular variation in the backward-photon region. It is much easier to calculate a "point" cross section for each photon counter, assuming that the photon is directed toward the center of the photon counter (Table I) and that the pion travels at 50.5° to the beam in the horizontal plane. Averaging the SPA over the acceptance by Monte Carlo calculations for photon energies between 10 and 50 MeV gives averaged cross-section values differing from the "point" calculation by no more than ±15% for the various photon counters, so that the "point" calculation is a reasonable first step for the comparison of theory with the data. When the cross sections for all 10 photon counters are combined (weighted by their geometrical solid angles), the difference between "point" and integrated cross sections is always less than 5%.

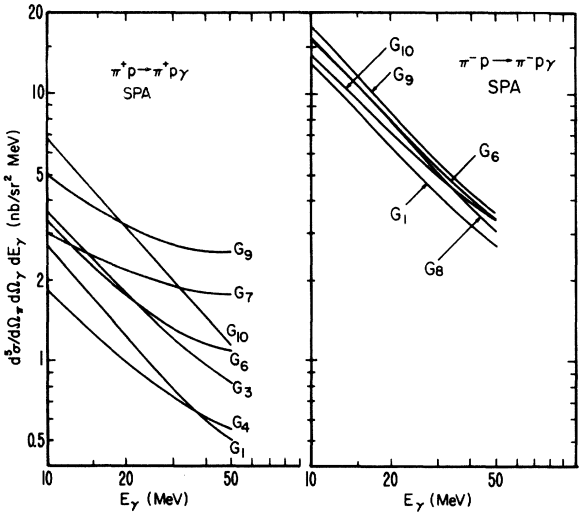

FIG. 14. Theoretical cross sections (lab) calculated using the soft-photon approximation (SPA), averaged over acceptances for individual photon counters. (a) $\pi^+p\to\pi^+p\gamma$. Curve for counter G_2 is similar to that for G_1; curve for G_5 similar to that for G_4; and curve for G_8 similar to that for G_7. (b) $\pi^-p\to\pi^-p\gamma$. The curves for counters G_2–G_5 and G_7 lie between those shown.

TABLE VI. Comparison of number of events found in each photon counter with predictions of the soft-photon approximation for $\pi^+p\to\pi^+p\gamma$. The errors are statistical and include background subtraction. In the χ^2 calculation, we take the standard deviation as the square root of the predicted number of events, adjusted for the average background subtraction.

Photon counter	E_γ = 15–20 MeV Theory	Exper.	E_γ = 20–30 MeV Theory	Exper.	E_γ = 30–40 MeV Theory	Exper.	E_γ = 40–50 MeV Theory	Exper.
1	4.6	1±2	7.3	9±4	5.1	7±3	4.2	7±3
2	5.5	3±3	8.9	8±4	6.3	9±3	5.1	5±2
3	7.4	12±4	12	16±5	9.1	11±3	7.7	15±4
4	4.1	1±2	7.3	7±3	5.8	5±2	5.2	10±3
5	4.7	5±3	8.4	2±3	6.6	9±3	5.8	7±2
6	6.9	9±3	13	9±3	11	6±3	9.7	9±3
7	8.5	8±3	17	12±4	16	11±3	16	3±2
8	9.8	10±4	20	13±4	19	9±3	18	7±3
9	12	11±4	25	27±5	24	16±4	23	12±4
10	13	13±4	21	27±5	15	22±5	12	11±3
All	77	73±11	140	130±13	117	105±11	106	86±10
χ^2 for 10 degrees of freedom	6.6		11.0		17.2		34.7	
χ^2 probability	0.76		0.36		0.07		0.0001	

B. Tests of the experiment

The credibility of the experimental data is supported by several considerations

(i) Elastic scattering measurements. The acceptance and efficiency of the pion and proton detection systems for low-photon-energy events, as well as most of the other normalization factors, are tested by measuring the differential cross section for $\pi^+ p$ and $\pi^- p$ elastic scattering with our apparatus. Data for these reactions were taken in separate runs with the photon counters removed from the trigger logic. The angular acceptance of the pion spectrometer was centered on a pion angle of 52° in the lab (with a width of ±5°), corresponding to 69° in the CMS. The resulting CMS cross sections are

$$\frac{d\sigma}{d\Omega^*}(\pi^+ p \to \pi^+ p) = 5.9 \pm 0.4 \text{ mb/sr}$$

$$\frac{d\sigma}{d\Omega^*}(\pi^- p \to \pi^- p) = 0.91 \pm 0.05 \text{ mb/sr}$$

where

$T = 298$ MeV,

$\theta^* = 69°$.

The errors are predominantly nonstatistical. Recent phase-shift solutions[15] give the corresponding values 5.23 mb/sr (π^+) and 0.93 mb/sr (π^-), averaged over the finite aperture. The agreement is consistent with the estimated errors, and is well within the tolerances set by the large statistical errors in the radiative scattering data.

(ii) π^0 production. A crude check on normalization is also provided by the detected events of the reaction $\pi^\pm p \to \pi^\pm p \pi^0$, which appears as a prominent peak in the distribution of neutral particle missing mass (Fig. 8). An order-of-magnitude calculation of the total cross section can be made by assuming isotropy in the CMS. The results are

$$\sigma(\pi^+ p \to \pi^+ p \pi^0) = 0.12 \pm 0.05 \text{ mb}$$

$$\sigma(\pi^- p \to \pi^- p \pi^0) = 0.11 \pm 0.05 \text{ mb}$$

where

$T = 298$ MeV.

These can be compared with a crude interpolation of the published total cross sections (themselves not very precise),[16] yielding approximately 0.11 ± 0.04 mb and 0.11 ± 0.06 mb for the π^+ and π^- reactions, respectively. Since the kinematics of a π^0-production event are similar to those of a radiative event with very high photon energy, this comparison tests the system's acceptance at the high-E_γ end of the spectrum.

(iii) Soft-photon limit. Probably the best confirmation of the measurements is the good agreement with the predictions of the soft-photon approximation in the region below 30 MeV where the Low theorem is expected to be applicable. It should be noted that this is the region in which the efficiency of the photon detectors is lowest and most uncertain; at higher energies their performance should not be a source of concern.

V. DISCUSSION OF RESULTS

The most prominent features of the experimental results are (i) good agreement with the soft-photon approximation for photons with energies below about 30 MeV, and (ii) a structureless, monotonic decrease in the cross section with photon energy, in contradiction with theoretical predictions.

A. Soft-photon approximation

For photon energies below 30 MeV, the data are in agreement with SPA predictions for both π^+ and π^-. The photon energy dependence averaged over the 10 counters is shown in Fig. 13. Table VI gives a detailed comparison, counter by counter, between our data and the SPA predictions. The agreement is good up to $E_\gamma = 30$ MeV, but deteriorates rapidly at higher photon energies. The comparison provides a determination of the range of validity of the Low theorem for radiative πp scattering.

Above 30 MeV, the largest discrepancies occur in those counters (G_7, G_8, G_9) for which the SPA theoretical cross section becomes flattest with photon energy (Fig. 14). In this region, the data for these counters are consistently low, implying that the energy dependence for the various counters is more nearly uniform than the SPA predicts.

One of the significant aspects of the geometry chosen for this experiment is the possibility of investigating the behavior of pions and protons far off the mass shell. In each of the "external" radiation diagrams of Fig. 1, the emission of the photon by an incident or outgoing pion or proton leaves a virtual particle whose "mass" varies with photon energy. The extent of this phenomenon is shown in Figs. 15(a) and 15(b), in which the ratio of each virtual particle's invariant mass squared to its rest mass squared is plotted as a function of photon energy for the conditions of the experiment. At $E_\gamma = 30$ MeV, the pion is already off the mass shell by more than its rest mass, in either the spacelike or timelike direction. It is therefore interesting that our experiment indicates that the Low theorem is applicable all the way up to this

photon energy.

The expected range of validity of the Low theorem or the soft-photon approximation has not been discussed in detail in the literature, although some consideration has been given by Feshbach and Yennie.[17] It is clear that our experiment probes the off-mass-shell effects significantly farther than existing proton-proton bremsstrahlung experiments which support the SPA.[18] The off-mass-shell behavior of the pion-nucleon interaction is fundamental to modern calculations of the nucleon-nucleon interaction.[5] The presence of the photon as a weak "probe" of the strong interaction makes radiative pion-proton scattering a good source of information on these off-mass-shell effects. Unfortunately this approach has not yet been explored extensively.

B. Comparison with specific theoretical predictions

Several published theoretical calculations of $\pi^+ p$ bremsstrahlung, when evaluated at our energy, predict a prominent bump near 60 MeV, the photon energy at which the outgoing pion and proton have an invariant mass near the resonant energy of 1236 MeV [see Fig. 15(c)]. Kondratyuk and Ponomarev[6,8] use a simple isobar model to derive an effective Lagrangian for the process in the resonance region. Fischer and Minkowski[13,14] provide an extension of the soft-photon formalism of Low. The results of these two models, shown in Fig. 13 as averaged over our 10 photon detectors, are qualitatively similar, but disagree drastically with the data in the hard-photon region. In both calculations, we assume the SU(6) quark model value for the magnetic moment of the $\Delta^{++}(1236)$. Setting $\mu(\Delta^{++})=0$ increases the height of the peak in the Kondratyuk-Ponomarev model and decreases it in the Fischer-Minkowski model; the difference is due to differing signs of the counterterms used to satisfy gauge invariance [Fig. 1(e)] in the two models.

No detailed comparison is made with the predictions of Baier, Pittner, and Urban.[19] We note only that these authors, like those mentioned above, predict a clear manifestation of the $\Delta^{++}(1236)$ in the form of a "bump" in the photon spectrum, which is absent in our experiment.

C. Other general approaches

After the publication of our preliminary results, Thompson[20] reported calculations based on the simple model of a Schrödinger, nonrelativistic current operator for radiative $\pi^+ p$ scattering. The model provides a mechanism which suppresses the influence of the $\Delta^{++}(1236)$ resonance on the photon spectrum. The calculation is not quantitative, in that the proton is treated as a spinless particle at rest, and the large but delicate cancellation of the pion and proton radiation is approximated by a constant scale factor. Thus a detailed comparison

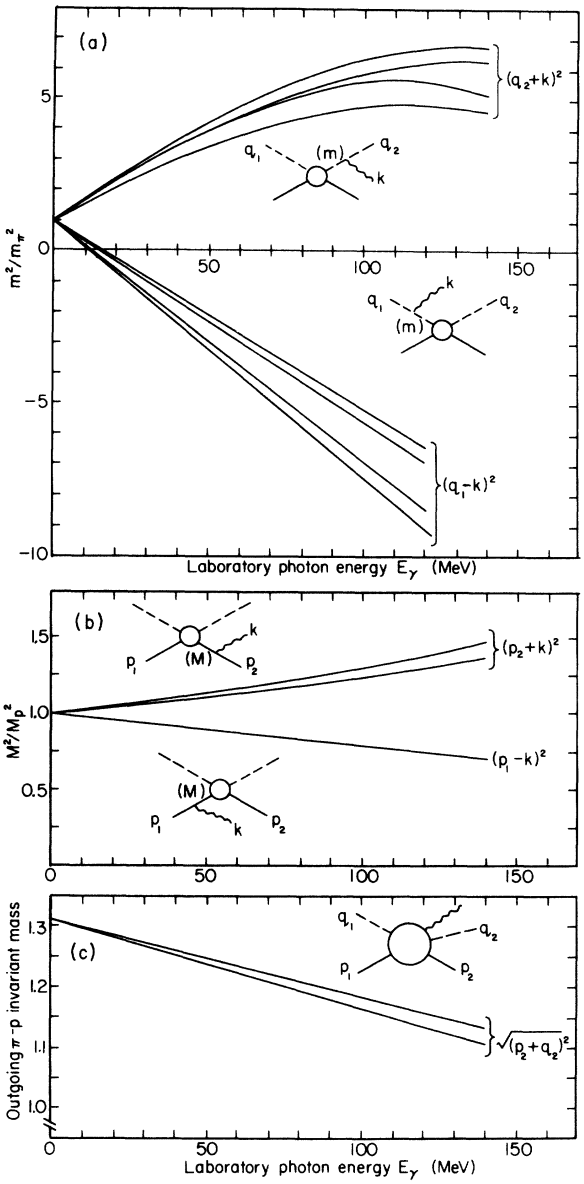

FIG. 15. Dependence of invariant kinematic quantities on photon energy for an incident kinetic energy of 298 MeV and the geometry of this experiment. Each graph shows the limits of the curves for the individual photon counters. (a) Invariant mass squared of the virtual pion, divided by $(139.6\ \text{MeV})^2$. (b) Invariant mass squared of the virtual proton, divided by $(938\ \text{MeV})^2$. (c) Invariant mass in GeV of the outgoing pion-proton system (which passes through the resonant energy of 1236 MeV near $E_\gamma = 60$ MeV).

with our data is not possible.

Haddock and Leung[21] have proposed a set of "hard-photon theorems" for pion-proton bremsstrahlung in the energy region of the present experiment. They conclude that a much more extensive set of measurements at other energies and photon angles is necessary before specific off-mass-shell properties can be extricated from the other theoretical uncertainties in the problem. Similarly, the extraction of the $\Delta^{++}(1236)$ magnetic moment must await an improved general understanding of the radiative πp scattering process.

D. Heuristic model

Prompted by the gross difference between the specific theoretical predictions and our experimental finding of a structureless photon spectrum, we have searched for a simple model that describes our data and agrees with the SPA in the limit of low photon energy. We have attempted several simple heuristic descriptions that agree approximately with the data but lack a known physical basis at present. We present only the simplest such description, in which the radiative scattering cross section in the c.m. system is set equal to $A\beta/k$, where k is the photon energy in the c.m. system, β is the slowly varying phase-space function of Eq. (4), and A is a *constant* coefficient, calculated from the limit of the leading term of the SPA expansion [Eq. (5a)] as $k \to 0$. [From Eqs. (3) and (4), it follows that the matrix element is then equal to a constant divided by k.] Since, at a given photon angle, the lab photon energy E_γ is proportional to k, and both β and the c.m.-to-lab transformation factor are very slowly varying with photon energy, this model gives a lab cross section which is nearly proportional to $1/E_\gamma$. The results of this calculation are shown in Fig. 13 labeled $1/k$, together with the data.

The agreement with the π^- data is good. For the π^+ data, there is only qualitative agreement with the $1/k$ calculation. This result is perhaps not surprising, in view of the differences in energy dependence calculated for individual photon counters in the SPA (Fig. 14). In the preliminary report on our results,[10] we stated that the $1/k$ fit was satisfactory. The difference in our conclusions is due to changes in the detailed evaluation of the $1/k$ "model" for our geometry.

VI. CONCLUSIONS

Our measurement of radiative pion-proton scattering at 298 MeV incident energy and backward photon angles has shown that a soft-photon-approximation calculation, based on the Low theorem, is valid for photon energies up to 30 MeV, an energy at which the radiating pion or proton is already substantially off the mass shell. At higher photon energies, the cross section falls monotonically with E_γ, and fails to show any qualitative manifestation of the $\Delta^{++}(1236)$ resonance, in contradiction to several recent theoretical predictions.

From the discussion of Sec. V, it should be abundantly clear that the extraction of the magnetic moment of the $\Delta^{++}(1236)$, one of the original objectives of our experiment, must await an improved general understanding of the radiative pion-proton scattering process.

A more extensive measurement of the pion-proton bremsstrahlung cross section at other incident energies and photon angles is now in progress, and results will be presented in forthcoming papers. We hope that, in the interim, the appearance of these unexplained results at backward photon angles will be a stimulus to better theoretical understanding of the process.

ACKNOWLEDGMENTS

We gratefully acknowledge the hospitality extended to us at the Lawrence Berkeley Laboratory, and the skillful help of Jimmy Vale and the crew of the 184-in. cyclotron. We thank Ray Belisle, Chris May, and Gary Segal for assistance in the assembly of the apparatus, Martin Thimel for his contributions to the computer programming, and Dr. Paul Glodis, Craig Ballagh, David Smith, and Stanley Jarrett for their assistance with portions of the analysis. We appreciate theoretical discussions with Dr. Peter Minkowski.

APPENDIX

In this appendix, we present the soft-photon approximation (SPA) formulas for the differential cross section for $\pi^+ p \to \pi^+ p\gamma$. The details will be omitted and the interested reader is referred to the original paper by Low.[3]

In the center-of-mass system, the initial pion and proton four-momenta are denoted by q_1, p_1, the corresponding outgoing four-momenta by q_2, p_2, and the photon four-momentum by k, so that

$$p_1 + q_1 = p_2 + q_2 + k\,. \tag{A1}$$

We choose the following invariants:

$$\begin{aligned} &s_1 = (p_1 + q_1)^2, \quad s_2 = (p_2 + q_2)^2, \quad s = \tfrac{1}{2}(s_1 + s_2)\,, \\ &t_1 = (q_2 - q_1)^2, \quad t_2 = (p_2 - p_1)^2\,. \end{aligned} \tag{A2}$$

In the following, we treat the external pion and proton charge radiation separately.

1. Pion charge radiation

Let $T(s, t, m_1^2, m_2^2)$ be the pion-proton scattering amplitude with m_1 and m_2 denoting the incoming and outgoing pion masses. For an elastic scattering $m_1^2 = m_2^2 = \mu^2$. The invariant quantity t is taken to be the momentum transfer to the nonradiating charged particle.

In terms of T, the amplitude for radiation from the pion can be written as

$$M_\mu^{(1)}\epsilon_\mu = \frac{q_2\cdot\epsilon}{q_2\cdot k}\,T(s_1, t_2, (q_2+k)^2, \mu^2) - \frac{q_1\cdot\epsilon}{q_1\cdot k}\,T(s_2, t_2, \mu^2, (q_1-k)^2). \tag{A3}$$

Gauge invariance requires that we add a term $M_\mu^{(2)}\epsilon_\mu$ in such a way that

$$M_\mu k_\mu = (M_\mu^{(1)} + M_\mu^{(2)})k_\mu = 0$$

or

$$M_\mu^{(2)}k_\mu = -M_\mu^{(1)}k_\mu\,. \tag{A4}$$

The amplitude for πp scattering with one pion off-mass-shell does not introduce any extra invariant amplitudes and can be written as

$$T(s_1, t, (q_2+k)^2, \mu^2) = A(s_1, t, (q_2+k)^2, \mu^2) + \tfrac{1}{2}(\not q_1 + \not q_2 + \not k)B(s_1, t, (q_2+k)^2, \mu^2)\,,$$

where $\not q = q_\mu\gamma_\mu$ and $\not k = k_\mu\gamma_\mu$ (γ_μ are the Dirac γ matrices).

To get $M_\mu k_\mu$, we expand A and B with respect to the variables and retain only the first derivatives, keeping only terms of first order in k. The algebra is messy, and we write down only the final form:

$$M_\mu^{(1)}k_\mu = 2(p_1+q_1)\cdot k\left[\frac{\partial A}{\partial s}(s, t_2, \mu^2, \mu^2) + \tfrac{1}{2}(\not q_1 + \not q_2)\frac{\partial B}{\partial s}(s, t_2, \mu^2, \mu^2)\right] + \not k B(s, t_2, \mu^2, \mu^2). \tag{A5}$$

Replacing k_μ by ϵ_μ will give us the desired $-M_\mu^{(2)}\epsilon_\mu$. The total amplitude is given by

$$M_\mu\epsilon_\mu = \left(\frac{q_2\cdot\epsilon}{q_2\cdot k} - \frac{q_1\cdot\epsilon}{q_1\cdot k}\right)T(s, t_2, \mu^2, \mu^2) + \left(\frac{q_1\cdot\epsilon}{q_1\cdot k}\,p_1\cdot k + \frac{q_2\cdot\epsilon}{q_2\cdot k}\,p_2\cdot k - p_1\cdot\epsilon - p_2\cdot\epsilon\right)\left[\frac{\partial A}{\partial s} + \frac{1}{2}(\not q_1 + \not q_2)\frac{\partial B}{\partial s}\right] + \frac{1}{2}\left(\frac{q_2\cdot\epsilon}{q_2\cdot k}\not k + \frac{q_1\cdot\epsilon}{q_1\cdot k}\not k - 2\not\epsilon\right)B(s, t_2, \mu^2, \mu^2). \tag{A6}$$

The term which falls off as $1/k$ in the above formula is of the form

$$\left(\frac{q_2\cdot\epsilon}{q_2\cdot k} - \frac{q_1\cdot\epsilon}{q_1\cdot k}\right)T(s, t_2, \mu^2, \mu^2)\,.$$

Notice that T is calculated at an averaged energy $s = \frac{1}{2}(s_1 + s_2)$, which means that its value changes as we move away from the region of $k \approx 0$.

2. Proton charge radiation

This particular case has been worked out completely in Ref. 3 and will not be repeated here. We give only the final result:

$$M_\mu^{(3)}\epsilon_\mu = \bar u(p_2)\left[(\gamma_\mu + \lambda\sigma_{\mu\nu}k_\nu)\frac{1}{\not p_2 + \not k - m}\,T + T\frac{1}{\not p_1 - \not k - m}(\gamma_\mu + \lambda\sigma_{\mu\nu}k_\nu) + \left(\frac{q_2\cdot k}{p_2\cdot k}\,p_2\cdot\epsilon - q_2\cdot\epsilon + \frac{q_1\cdot k}{p_1\cdot k}\,p_1\cdot\epsilon - q_1\cdot\epsilon\right)\frac{\partial T}{\partial s}\right]u(p_1)\,, \tag{A7}$$

where λ is the proton's anomalous moment, and $T = T(s, t_1, M^2, M^2)$, with M being the proton mass.

3. Cross-section calculation

The total external bremsstrahlung amplitude is the sum of Eq. (A6) and Eq. (A7):

$$M_\mu^{\text{total}}\epsilon_\mu = M_\mu\epsilon_\mu + M_\mu^{(3)}\epsilon_\mu\,. \tag{A8}$$

The total cross section for $\pi p \to \pi p\gamma$ is given by

$$\sigma = \frac{e^2}{(2\pi)^5}\,\frac{1}{|\vec V_{12}|(2\omega_1)(E_1/M)}\int\frac{d^3k}{2k}\,\frac{d^3q_2}{2\omega_2}\,\frac{d^3p_2}{(E_2/M)}\,\delta^4(\textstyle\sum p_i)\sum_{\text{spins}}|M_\mu\epsilon_\mu|^2\,, \tag{A9}$$

where $|\vec{V}_{12}|$ is the relative velocity between the two incoming particles, and

$$p_1^\mu = (E_1, \vec{p}), \quad p_2^\mu = (E_2, \vec{p}),$$

$$q_1^\mu = (\omega_1, \vec{q}_1), \quad q_2^\mu = (\omega_2, \vec{q}_2),$$

$$k^\mu = (k, \vec{k}).$$

Choosing the five independent variables to be $d\Omega_\pi$, $d\Omega_k$, dk, we can integrate over the remaining four variables, and obtain

$$\frac{d^5\sigma}{d\Omega_\pi d\Omega_\gamma dk} = \frac{\alpha M^2}{64\pi^4} k \frac{|\vec{q}_2|}{|\vec{q}_1| W |W - k + (\omega_2/|\vec{q}_2|^2)\vec{q}_2 \cdot \vec{k}|} \times \sum_{\text{spins}} |M_\mu \epsilon_\mu|^2 . \tag{A10}$$

W is the total CMS energy, and all quantities are calculated in the CMS. The phase-space function β referred to in Eq. (4) of the Introduction is given by

$$\beta = \alpha \frac{M^2}{64\pi^4} \frac{|\vec{q}_2|}{|\vec{q}_1| W |W - k + (\omega_2/|\vec{q}_2|^2)\vec{q}_2 \cdot \vec{k}|} . \tag{A11}$$

Figure 2(a) shows the contributions of various terms in Eq. (A8), calculated for the geometry of photon counter G_4. In this figure the curve labeled "π only" is calculated from Eq. (A6), the radiation due to the pion. The curve labeled "p only" shows the radiation due to the proton, given by Eq. (A7). Curve β is calculated from Eq. (A11). Curve I is the first term from Eq. (5b), while curve II gives the first two terms of Eq. (5b). Note that this curve shows a negative "cross section" when b is large and of opposite sign to a; the danger in truncating such a "power series" to simplify calculations should be obvious. Finally, curve σ shows Eq. (5a) with $c = 0$, which is the soft-photon-approximation calculation of the differential cross section. Figure 2(b) shows the same quantities for the reaction $\pi^- p \to \pi^- p\gamma$.

Some comments on these figures are in order.

(1) The $\pi^+ p$ radiative cross section in this kinematic region is considerably smaller than the $\pi^- p$, although the contributions due to the individual radiating particles are larger in the $\pi^+ p$ reaction owing to the larger elastic scattering cross sections. This phenomenon is due to the fact that for backward-photon kinematics, the pion and proton radiation terms interfere destructively for $\pi^+ p$ and constructively for $\pi^- p$.

(2) In the soft-photon region below $E_\gamma = 40$ MeV, the cross section is closely approximated by the leading terms of Eq. (5b), which is proportional to $1/E_\gamma$. The coefficient of this term, it should be noted, *is not independent of* E_γ except in the limit $E_\gamma \to 0$.

(3) In the SPA, both the π^+ and π^- cross sections rise steeply with increasing photon energy above $E_\gamma \approx 80$ MeV. This rise is due to the breakdown of the linear approximation used in describing the elastic scattering amplitude, which occurs when the outgoing pion-proton system has an invariant mass near the resonant energy of 1236 MeV. $\sqrt{s_2} = 1236$ MeV when the photon energy in the lab is about 55 MeV in our geometry. Thus the presence of the $\Delta(1236)$ restricts the range of usefulness of the SPA to photon energies below this value.

---

*Work performed under the auspices of the U. S. Atomic Energy Commission.

†Present address: Department of Physics, Pahlavi University, Shiraz, Iran.

‡Present address: State University of New York at Buffalo, Buffalo, N. Y. 14222.

§Present address: Computer Sciences Corp., Silver Spring, Md. 20910.

‖Present address: Computer Sciences Corp., Falls Church, Va. 22046.

¶Present address: Oximetrics, Mountainview, Calif. 94040.

[1] J. D. Bjorken and S. D. Drell, *Relativistic Quantum Mechanics* (McGraw-Hill, New York, 1964), Chap. 7.

[2] We shall designate the photon energy in the center-of-mass system by k and the laboratory photon energy by E_γ. At a given photon angle, they are exactly proportional. Under the conditions of the present experiment, $k = (1.15\text{–}1.35)E_\gamma$.

[3] F. E. Low, Phys. Rev. 110, 974 (1958).

[4] T. H. Burnett and N. M. Kroll, Phys. Rev. Lett. 20, 86 (1968); S. L. Adler and Y. Dothan, Phys. Rev. 151, 1267 (1966); J. S. Bell and R. Van Royen, Nuovo Cimento 60A, 62 (1969).

[5] G. E. Brown, in *High-Energy Physics and Nuclear Structure*, edited by G. Tibell (North-Holland, Amsterdam, 1974), pp. 3–8.

[6] L. A. Kondratyuk and L. A. Ponomarev, Yad. Fiz. 7, 111 (1968) [Sov. J. Nucl. Phys. 7, 82 (1968)].

[7] V. L. Zacharov, L. A. Kondratyuk, and L. A. Ponomarev, Yad. Fiz. 8, 783 (1968) [Sov. J. Nucl. Phys. 8, 456 (1969)].

[8] A. P. Vanzha and M. M. Musakhanov, Dubna Report No. JINR-P2-6305, 1972 (unpublished). This paper corrects an omission in the counterterms, which restore gauge invariance, in Ref. 6.

[9] B. T. Feld, *Models of Elementary Particles* (Blaisdell, Waltham, Mass., 1969), Chap. 15.

[10]M. Arman, D. J. Blasberg, R. P. Haddock, K. C. Leung, B. M. K. Nefkens, B. L. Schrock, D. I. Sober, and J. M. Sperinde, Phys. Rev. Lett. 29, 962 (1972).
[11]M. Arman, Ph.D. thesis, University of California, Los Angeles, 1972 (unpublished).
[12]D. I. Sober, M. Arman, D. J. Blasberg, R. P. Haddock, K. C. Leung, and B. M. K. Nefkens, Nucl. Instrum. Methods 108, 573 (1973).
[13]W. E. Fischer and P. Minkowski, Nucl. Phys. B36, 519 (1972).
[14]P. Minkowski, private communication.
[15]CERN - Kirsopp solution (1968), quoted in D. J. Herndon *et al.*, Berkeley, Calif., Report No. UCRL-20030 πN, 1970 (unpublished).
[16]Data compilation in M. G. Olsson and G. B. Yodh, Phys. Rev. 145, 1309 (1966).
[17]H. Feshbach and D. R. Yennie, Nucl. Phys. 37, 150 (1962).
[18]E. M. Nyman, Phys. Rep. 9C, 179 (1974).
[19]R. Baier, L. Pittner, and P. Urban, Nucl. Phys. B27, 589 (1970).
[20]R. H. Thompson, Nuovo Cimento 16A, 290 (1973).
[21]R. P. Haddock and K. C. Leung, Phys. Rev. D 9, 2151 (1974).

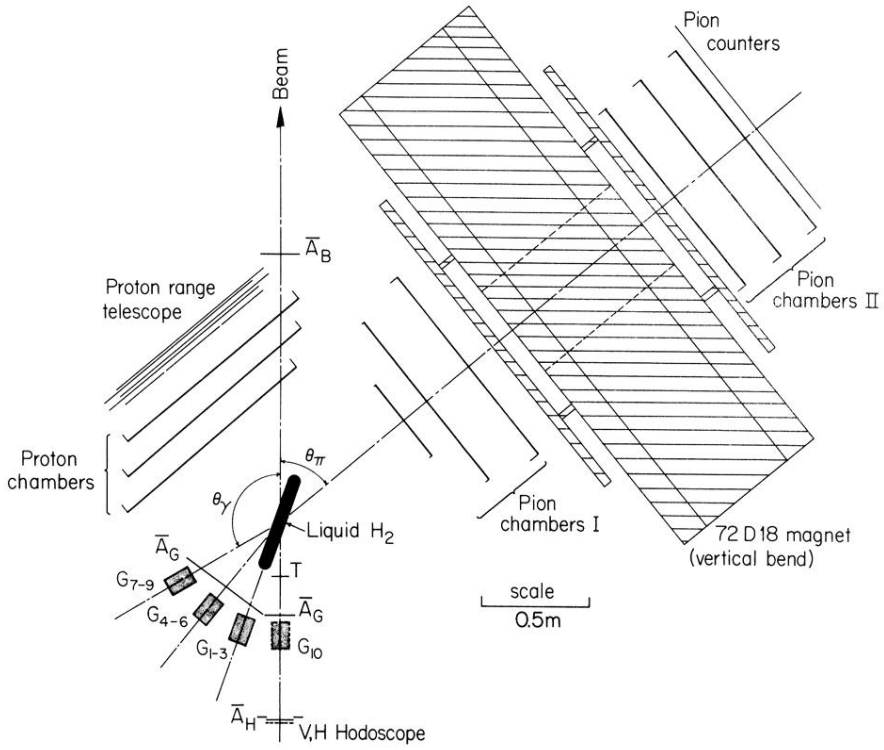

FIG. 4. Experimental apparatus. G_1 through G_{10} are the lead-glass photon counters, of which only G_1, G_4, and G_7 lie in the horizontal plane. Dimensions are given in Table I.